PAPER

Check for updates

Electropolymerization of Au nanoparticle incorporated poly(dopamine) thin-films at a micro liquid|liquid interface

Leila Nazari,[a] Fanqi Kong, [ID] [b] E. Bradley Easton [ID] [b] and Talia Jane Stockmann [ID] *[a]

Dopamine (DA) is an important biomolecule of the central nervous system (CNS) as well as a monomer incorporated into melanin, a macromolecule often associated with skin pigmentation. Herein, we have investigated the electropolymerization of DA to form polydopamine (PDA) at a micro interface between two immiscible electrolyte solutions (micro-ITIES) between water|1,2-dichloroethane (w|DCE) under external, electrochemical control. DA oxidation to form PDA was achieved *via* the use of an ionic liquid composed of trihexyltetradecylphosphonium (P_{66614}) paired with $AuCl_4^-$ and dissolved in the DCE phase. $AuCl_4^-$ acts as a strong oxidizer, accepting electrons from DA to form Au nanoparticles (NPs) that become incorporated into the growing PDA matrix. Au NP/PDA electrosynthesis was found to improve with increasing aqueous phase pH and was discovered to create a delicate, free-standing film. Au NP/PDA was used to modify a glassy-carbon electrode (GCE) and employed as a platform for DA detection. This proof-of-concept DA-biosensor demonstrated quasi-reversible DA oxidation and a good limit-of-detection (LOD) and linear-dynamic-range of 0.27 μM and 0.2–20 μM, respectively, using differential pulse voltammetry (DPV).

Introduction

Dopamine (DA) is ubiquitous in nature, often found as a neurotransmitter that participates in most cognitive or movement control events in humans[1] within the central nervous system (CNS). It can also be found outside the CNS and is the chemical basis of melanin, including eumelanin, pheomelanin, and neuromelanin.[2,3] DA is synthesized by the body from tyrosine, which is first converted to L-3,4-dihydroxyphenylalanine, a.k.a. Levodopa (L-DOPA), before being transformed to DA. Melanin is a heterogeneous polymer that can appear dark brown to black or even yellow.[2] Eumelanin is composed of monomers of 5,6-dihydroxyindole (DHI) and 5,6-dihydroxyindole-2-carboxylic acid (DHICA).[4] The formation of DHI is achieved through an intramolecular 1,4-Michael addition of the amine towards the catechol ring within DA. DHICA is similarly generated, however, from L-DOPA. All of these are derivatives of DA; thus, melanin, a complex macromolecule is partially composed of polydopamine (PDA). Polymerization off of the aromatic, catechol ring can generate a conductive polymer. Neuromelanin, a heteropolymer composed partly of the monomer DHI, has been found in the *substantia nigra* of the

brain, and its loss or degradation has been linked to Parkinson's[5] and Alzheimer's[6] diseases. Melanin coordinates well to metal ions, including Fe, Cu, and some heavy metals like Pb or Hg,[7] through the hydroxyl groups of the catechol moiety. It has been proposed that neuromelanin may act as a protective barrier for the brain by coordinating to these metal ions that are toxic to neurons. However, as neuromelanin breaks down, this protection is lost, potentially leaking toxic metal ions into neural tissue.[7]

Outside the CNS, different variations of melanin are employed throughout the animal kingdom as skin pigmentation[8] owing to their broad optical absorption cross-section that inhibits radiative cell damage. Since the discovery of PDA as an adhesive coating on mussels,[9] it has been increasingly employed in anti-corrosion, materials science studies,[10,11] and even as an energy storage material.[12] Meanwhile, the detection of DA for neuroscience investigations has been of critical importance for decades.[13] In the 1980s, Wightman and Ewing developed carbon fiber microelectrodes[14–16] as *in vivo* electroanalytical probes to directly measure DA. This has since been extended to the nanoscale, particularly for the real-time monitoring of chemical communication through fundamental understanding of exocytosis.[17]

A number of *in vitro* analytical methods have arisen for DA quantification, including exploiting the inherent fluorescence of PDA,[18,19] or *via* liquid chromatography-mass spectroscopy,[20] as well as many other approaches that often combine two or more sensing platforms.[21] Nevertheless, electrochemical

[a]*Department of Chemistry, Core Science Facility, Memorial University of Newfoundland, 45 Artic Ave, St. John's, NL, A1C 5S7, Canada. E-mail: tstockmann@mun.ca*

[b]*Electrochemical Materials Lab, Faculty of Science (Chemistry), Ontario Tech University, 2000 Simcoe North, Oshawa, ON L1G 0C5, Canada*

detection is the only present method for real-time monitoring *in vivo*. Shao's group demonstrated that DA could be detected at an interface between two immiscible electrolyte solutions (ITIES) through facilitated ion transfer reactions employing 18-crown-6 ether, while ensuring that DA was in a protonated, charged state.[22] More recently, Shen's group[23] employed a nano-ITIES between 2-nitrophenyl octyl ether (NPOE) and water for the detection of another neurotransmitter, acetylcholine, through simple ion transfer. The ITIES was considered advantageous for two predominant reasons. First, on unmodified electrodes, DA oxidation is often irreversible and can cause fouling of the electrode surface through the formation of PDA – this cannot happen at a liquid|liquid interface when DA undergoes simple or facilitated ion transfer.[24] Second, DA oxidation occurs in roughly the same potential region as other common biomolecules, particularly ascorbic acid (AA) and uric acid (UA), that can interfere with its quantification;[25–27] this type of interference is overcome at the liquid|liquid interface since the charge transfer mechanism is fundamentally different to a redox process. Research has continued at the solid/electrolyte interface using modified electrodes. Electrodes incorporating conjugated, aromatic systems such as graphene or graphene oxide have been shown to improve the electrochemical reversibility of DA oxidation as well as enhance the selectivity and sensitivity of the electrochemical sensing platform.[27–30] This can also be achieved *via* inclusion of metal nanoparticles (NPs) such as Au.[31] These platforms often rely on modifying glassy carbon electrodes (GCEs). GCEs are advantageous as they have very low background currents and are poor electrocatalysts; this provides a good baseline, since any enhancement is brought about by the modification itself. For *in vivo* continuous neurotransmitter monitoring, however, this is not ideal since hard, rigid objects like the GCE or Pt ultramicroelectrodes, such as the ones used in deep-brain-stimulation (DBS) in the treatment of Parkinson's disease, could be isolated from the body by scar tissue.[32] This has the potential to limit the long-term efficacy of DBS.[32,33] So, research into soft polymer electrodes for bioimplantation has become a focus.[34]

Electropolymerization of conductive polymer films at a liquid|liquid interface offers several advantages over solid/electrolyte ones. Any film formed at a solid electrode will be influenced by its baseline surface morphology, and it cannot be removed without significantly damaging the film. This is not the case at a liquid|liquid interface; whereby, films are easily removed and used as free-standing electrodes.[34–41] Moreover, the liquid|liquid interface is molecularly sharp and smooth, so this likely exhibits little morphological influence on the film. Electrochemical control is achieved by externally manipulating the Galvani potential difference ($\Delta_{DCE}^{w}\phi$) across the water|oil (w|o) interface, $\phi_w - \phi_o = \Delta_{DCE}^{w}\phi$, using an electrode immersed in either phase.[42] Lehane *et al.*[34] demonstrated the electropolymerization of 3,4-ethyldioxythiophene (EDOT) at a large (cm scale) water|α,α,α-trifluorotoluene (w|TFT) interface using Ce^{4+}(aq) as the electron acceptor, which generated a free-standing PEDOT, conductive polymer film. Our group has explored the electrogeneration of nanocomposites through the simultaneous formation of Au and Cu metal NPs within
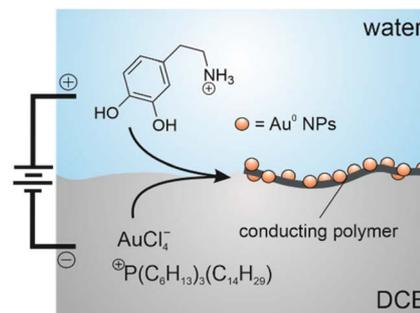
Scheme 1 Diagram of the interfacial electron transfer reaction taking place across the water|1,2-dichloroethane (w|DCE) micro-interface between AuCl$_4^-$ in DCE and dopamine (DA) in the aqueous phase, electrogenerating the conductive polymer/nanocomposite film.

a growing conductive polymer matrix using monomers such as 9-vinylcarbazole,[39] 2,2′:5′,2″-terthiophene (TT),[41,43] as well as more exotic molecules such as dithiafulvenyl-functionalized pyrenes.[40]

Herein, we investigated the electrogeneration of Au NP-incorporated PDA at a micro-ITIES. In this system, DA is dissolved in water and injected into the back of a specialized pipette holder. The pipette is composed of borosilicate glass with a pulled end that incorporates a ~500 μm long microchannel that is 25 μm in diameter.[40,44] The tip is then submerged inside a 1,2-dichloroethane (DCE) solution containing a hydrophobic Au salt, $P_{66614}AuCl_4$ (trihexyltetradecylphosphonium tetrachloroaurate) while the ITIES is maintained at the end of the microchannel. AuCl$_4^-$ acts as an excellent oxidizing agent, accepting electrons from DA in a heterogeneous electron transfer reaction across the ITIES (see Scheme 1). The Au NP/PDA film was successfully generated using cyclic voltammetry; however, it was also quite soft and fragile. It was removed from the interface by ejecting a droplet from the tip of the pipette using a syringe on the back of the specialized holder.[40,41] This was used to deposit the nanocomposite on a GCE to investigate its use as a DA biosensor. Here it showed a good limit-of-detection and linear range using differential pulse voltammetry (DPV).

Experimental

All chemicals were used as received unless described otherwise with aqueous solutions prepared using ultrapure water obtained from a MilliQ system (18.2 MΩ cm). Dopamine hydrogen chloride (≥98%), potassium tetrachloroaurate (KAuCl$_4$, >98%), 1,2-dichloroethane (DCE, ≥99.0%), trihexyltetradecylphosphonium bromide (P_{66614}Br, >95%) trioctylphosphine (>97%), bromooctane (99%), hydrochloric acid solution (HCl, >37%), potassium hydroxide (≥85%), potassium phosphate monobasic (≥99.0%), ferrocene methanol (FcCH$_2$-OH, 97%), and potassium phosphate dibasic (≥98%) were sourced from Sigma-Aldrich. Potassium chloride (KCl, 99.0%) was bought from ACP. Tetrakis(pentafluorophenyl)borate lithium etherate (LiTB, ≥99%) was obtained from Boulder Scientific. The ionic liquid (IL) P_{8888}TB (tetraoctylphosphonium

tetrakis(pentafluorophenyl)borate) was synthesized as described previously[45] and used as supporting electrolyte in the DCE phase.
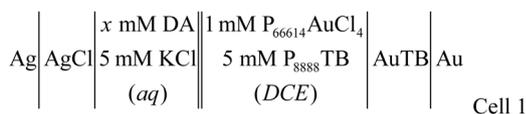
A second IL, trihexyltetradecylphosphonium tetrachloroaurate ($P_{66614}AuCl_4$), was prepared *via* a 1 : 1 metathesis reaction between $P_{66614}Br$ and $KAuCl_4$ dissolved in CH_2Cl_2. The reactants were allowed to stir overnight, and the reaction mixture was filtered under reduced pressure through Whatman filter paper, removing the solid KBr precipitate. The filtrate containing $P_{66614}AuCl_4$ was washed 3× with MilliQ water, then excess CH_2Cl_2 was removed on a roto-evaporator followed by drying on a Schlenk line under vacuum.

CHI6059 potentiostat from CH Instruments was used throughout for electrochemical measurements. Micro-interfacial experiments were conducted in 2-electrode mode using a micropipette installed within a specialized holder described previously by us.[40,41] The working electrode (WE) of the potentiostat was connected to an Ag wire (Delta Scientific) *via* a modified SMA connector integrated within the holder. The Ag wire was immersed in the aqueous solution which was back filled into the holder/capillary. An Au wire (Delta Scientific) was used as the counter/reference electrode (CE/RE) in the DCE phase. Unless otherwise indicated, the micro-ITIES was 25 μm in diameter and positioned at the tip of the micropipette. Scheme 2 describes the electrolytic cell employed at the micro liquid|liquid interface.

Glassy-carbon electrodes (GCE, CH Instruments) 4 mm outer diameter were employed for large, solid/solution electrode experiments in 3-electrode mode, whereby a Pt-wire counter and Ag/AgCl reference electrodes completed the cell. GCEs were tested with and without modification by the Au NP/PDA nanocomposite.

X-ray photoelectron spectroscopy was performed using a Thermo Scientific Nexsa instrument equipped with a monochromatic Al Kα X-ray source (1486.7 eV) and a 180° double focusing hemispherical analyser with a 128-channel detector with effective charge compensation. The instrument was equipped with a flood gun, which provides a steady flow of low-energy electrons to compensate plausible charging. The adventitious carbon peak at 284.8 eV was used to calibrate the binding energies.

A Varian 6000i UV-Vis-NIR and Bruker INVENIO-R spectrometers were used for UV-vis and FTIR studies, respectively.

Scanning electrochemical microscopy (SECM) was performed using an Elproscan (Heka Electroniks) in 3-electrode mode; whereby, an inlaid disc carbon fibre ultramicroelectrode (UME) served as the working electrode, Pt wire as counter, paired with an Ag/AgCl reference electrode.

Results and discussion

Scheme 1 depicts the electrosynthetic configuration; whereby, DA and $P_{66614}AuCl_4$ were dissolved in the aqueous and DCE phases, respectively. Owing to the intermediate hydrophobicity/hydrophilicity of $AuCl_4^-$,[39,40,44,48–51] it can partition from DCE to water and undergo homogeneous electron transfer, initiating bulk polymerization of DA. This partitioning is likely mitigated somewhat by the small interfacial size and experimental configuration that limits mixing during setup.[52] Liquid|liquid interfacial electropolymerization of DA was first explored voltammetrically. Fig. 1 shows the cyclic voltammogram (CV) recorded using Cell 1 without DA added to the aqueous phase. The pulse was initiated at roughly −0.15 V and swept towards positive potentials. A sigmoidal wave was observed with a half-wave potential ($\Delta_{DCE}^{w}\phi_{1/2}$) of 0.185 V which is the simple ion transfer of $AuCl_4^-$ from DCE → w.[44,48,50] The sharp increase in the current at ~0.6 V is the limit of the polarizable potential window (PPW) that is associated with the simple ion transfer of the supporting electrolyte; in this case, K^+ transfer from w → DCE as well as TB^- from DCE → w.[42,53] During the reverse pulse towards negative potentials, a peak-shaped wave was recorded with a peak-potential ($\Delta_{DCE}^{w}\phi_{p}$) ≈ 0.126 V which is $AuCl_4^-$ transfer back from w → DCE. If one assumes Randles-Ševčík-like behaviour,[54] then $\Delta_{DCE}^{w}\phi_{1/2} \approx \Delta_{DCE}^{w}\phi_{p} \pm (0.0285\ V) \times z^{-1} \approx 0.154$ V. Here, z is the charge of the ion undergoing transfer. The asymmetric ion transfer profile (peak-shaped from w → DCE, and sigmoidal from DCE → w) is due to the pipette's unique geometry, which results in linear diffusion inside and hemispherical diffusion outside.[55] Thus, the former resembles the signal profile common at larger electrodes, while the latter is more analogous to an inlaid-disc ultramicroelectrode (UME).
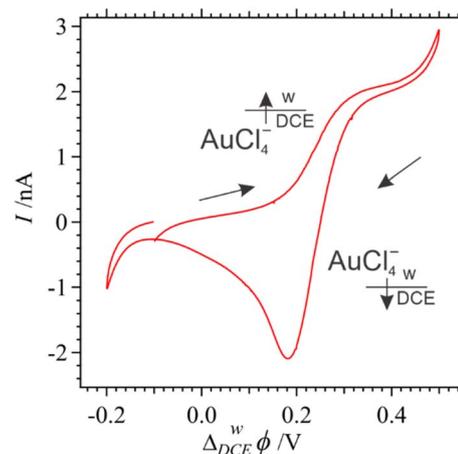
$$Ag \left| AgCl \left| \begin{matrix} x\ mM\ DA \\ 5\ mM\ KCl \\ (aq) \end{matrix} \right\| \begin{matrix} 1\ mM\ P_{66614}AuCl_4 \\ 5\ mM\ P_{8888}TB \\ (DCE) \end{matrix} \right| AuTB \left| Au \right.$$

Cell 1

Scheme 2 Electrochemical cell employed in which the double-bar has been used to emphasize the immiscible water|1,2-dichloroethane (w|DCE) micro-interface (25 μm in diameter); whereby, *x* mM of dopamine (DA) was added to the aqueous phase, while 1 mM of $P_{66614}AuCl_4$ (trihexyltetradecylphosphonium tetrachloroaurate) ionic liquid (IL) was added to the DCE phase along with 5 mM $P_{8888}TB$ (tetraoctylphosphonium tetrakis(pentafluorophenyl)borate) IL as supporting electrolyte. The pH of the aqueous phase was adjusted using aqueous solutions of HCl or KOH.

Fig. 1 Cyclic voltammogram (CV) obtained using Cell 1 with no DA added to the aqueous phase, *i.e.*, a blank CV, measured at 0.020 V s^{-1}.

Continuing to scan negatively, the other edge of the PPW is reached at roughly −0.3 V with an increase in the negative current signal associated with the ion transfer of the other supporting electrolyte components, *i.e.*, P_{8888}^+/P_{66614}^+ from DCE → w and Cl^- from w → DCE. These voltammetric results for simple ion transfer agree well with previous reports in which the micro-ITIES is positioned at the tip of a pulled glass capillary.[23,39,43,44,48,50,51] All voltammograms recorded at the liquid-|liquid interface have been referenced using the $AuCl_4^-$ ion transfer potential which was assumed to be $\Delta_{DCE}^w \phi_{AuCl_4^-}^{o'} = 0.126$ V.[44]

$AuCl_4^-$ can undergo ligand speciation with increasing pH above 2 forming $AuCl_{4-\gamma}(OH)_\gamma^-$; whereby, γ is the stoichiometric equivalents of Cl^- ligands replaced with OH^- which increases concomitantly with pH.[39,44,49,56] The presence of $AuCl_{4-\gamma}(OH)_\gamma^-$, however, results in a second ion transfer signal at slightly more negative potentials relative to that for $AuCl_4^-$. This was not observed at pH 2; however, as the pH was increased a second peak emerges at pH 8 and 10, while a third appears at pH 11.5, see Fig. S1 of the SI. These have been tentatively labelled as $AuCl_3OH^-$ and $AuCl_2(OH)_2^-$, respectively. Because $AuCl_4^-$ is present initially in the DCE phase, it will only undergo ligand speciation when it transfers into the water phase. The local pH in the vicinity of the ITIES may vary from the bulk. In the work of Luty-Błocho *et al.*,[57] $AuCl_4^-$, $AuCl_3OH^-$, $AuCl_2(OH)_2^-$, and $AuCl(OH)_3^-$ were calculated to be the dominant species at pH < 5, pH 6, pH 7, and pH > 9, respectively. Since only 3 peaks were observed over the course of increasing the pH, it was decided to label them according to the first Au ligand species described by Luty-Błocho *et al.* This is speculative and awaits future work incorporating tandem spectroscopy to confirm with certainty which peak – beyond that of $AuCl_4^-$ – belongs to which species.

Next, DA was added to the aqueous phase starting at a concentration of 20 mM while adjusting the pH of the aqueous phase *via* additions of HCl or KOH. Scheme 3 shows the 3-step deprotonation mechanism (reaction [1]) whose three pK_a's are 9.05, 10.58, and 12.07 as described by Sanchez-Riviera *et al.*[47] Thus, at pH < 9, H_3DA^+ (see Scheme 3) should be the dominant species, while at roughly pH 9–10, 10–13, and >13, H_2DA, HDA^-, and DA^{2-}, respectively, are the dominant protonation states. The remaining hydroxyl-proton is likely stabilized *via* hydrogen bonding to the adjacent –O^- for the H_2DA and HDA^- forms.[46] Also in Scheme 3 are reactions [2] and [3] which show the oxidation of DA to dopamine quinone (DAQ) as well as the intramolecular 1,4-Michael addition forming the indole,[58] respectively. Polymerization of DA is complex and still under scrutiny;[59,60] however, it likely occurs off of the 2, 3, 4, and 7 positions of the indole, *i.e.*, DHI and I56D, as well as the 3 and 6 positions of DA or DAQ.

Fig. 2 depicts the voltammograms recorded at 0.020 V s^{-1} while changing the pH of the aqueous phase from 2 to 11.5. Fig. 2A–C and G–I show the first voltammetric scan, while Fig. 2D–F and J–L plot each subsequent 5th scan up to the 20th. At pH's greater than 8 and in the presence of oxygen, it was observed that DA polymerized spontaneously in the aqueous phase forming a black precipitate that filled and clogged the
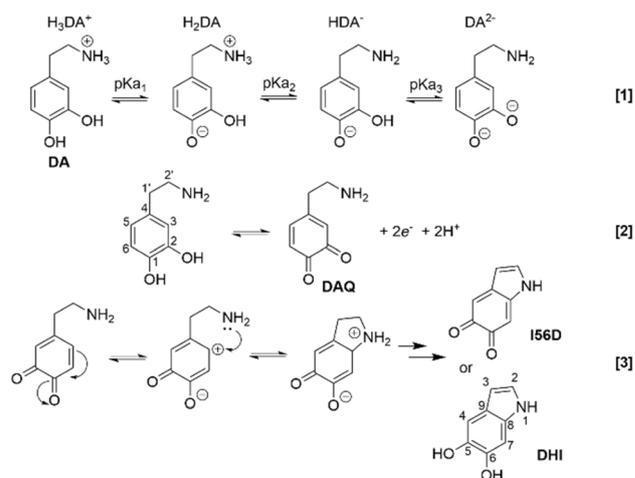
Scheme 3 Reaction [1] depicts the dopamine (DA) deprotonation mechanism with changing pH; whereby, pK_a's 1–3 are 9.05, 10.58, and 12.07 as reported by Sanchez-Riviera *et al.*[46,47] and the different protonated states have been labeled H_3DA^+ to DA^{2-}. Reaction [2] shows the 2-electron concerted oxidation of DA to dopamine quinone (DAQ) as well as the carbon numbering scheme within the DA molecule. Enolate formation and subsequent intramolecular 1,4-Micheal addition to form the indole has been drawn in reaction [3]. The numbering scheme for the indole is also given. Abbreviations: DHI = 5,6-dihydroxyindole; I56D: indole-5,6-dione.

pipette. This is in good agreement with previous reports of DA stability at high pH that has been exploited to coat surfaces in the past.[8,12,46,59,60] Thus, to ensure that PDA was not forming spontaneously,[46] the aqueous phase was purged with N_2 gas before adding DA and injecting the solution into the micropipette when operating at pH ≥ 5 just to err on the side of caution.

Examining Fig. 2A with the aqueous pH = 2, during the first voltammetric scan, the simple ion transfer signal for $AuCl_4^-$ transfer has been replaced by a sigmoidal wave in both positive and negative potential sweep directions at $\Delta_{DCE}^w \phi_{1/2} \approx 0.09$ V. After the first CV cycle, a peak-shaped wave grows with $\Delta_{DCE}^w \phi_P = 0.11$ V during the scan from positive to negative potentials. The peak-shaped wave quickly increases in current intensity achieving a magnitude of ~4 nA relative to the baseline current. This is consistent with the transfer of a negative charge from w → DCE. Thus, we hypothesize the initial steady-state voltammetric response is likely owing to heterogeneous electron transfer from DA(aq) to $AuCl_4^-$(DCE). It is also possible that the lack of a peak-shaped wave during the negative potential scan is owing to the homogeneous consumption of $AuCl_4^-$ through uncontrolled electropolymerization with DA after it transfers from DCE → w. After the initial scan, and owing to sluggish polymerization kinetics at low pH, the simple ion transfer wave for $AuCl_4^-$ re-emerges. If one assumes that DA donates 2 electrons and $AuCl_4^-$ accepts 3, then a general first step could be described using reaction 4 (see Scheme 4); whereby, $8Cl^-$ and $6H^+$ are effectively released to the DCE and w phases, respectively. The presence of 4 equivalents of Cl^- for each $AuCl_4^-$ reduced in the vicinity of the ITIES on the DCE side should result in a positive current offset in the voltammetric response; however, this was not observed (see Fig. 2). Thus, it is likely that
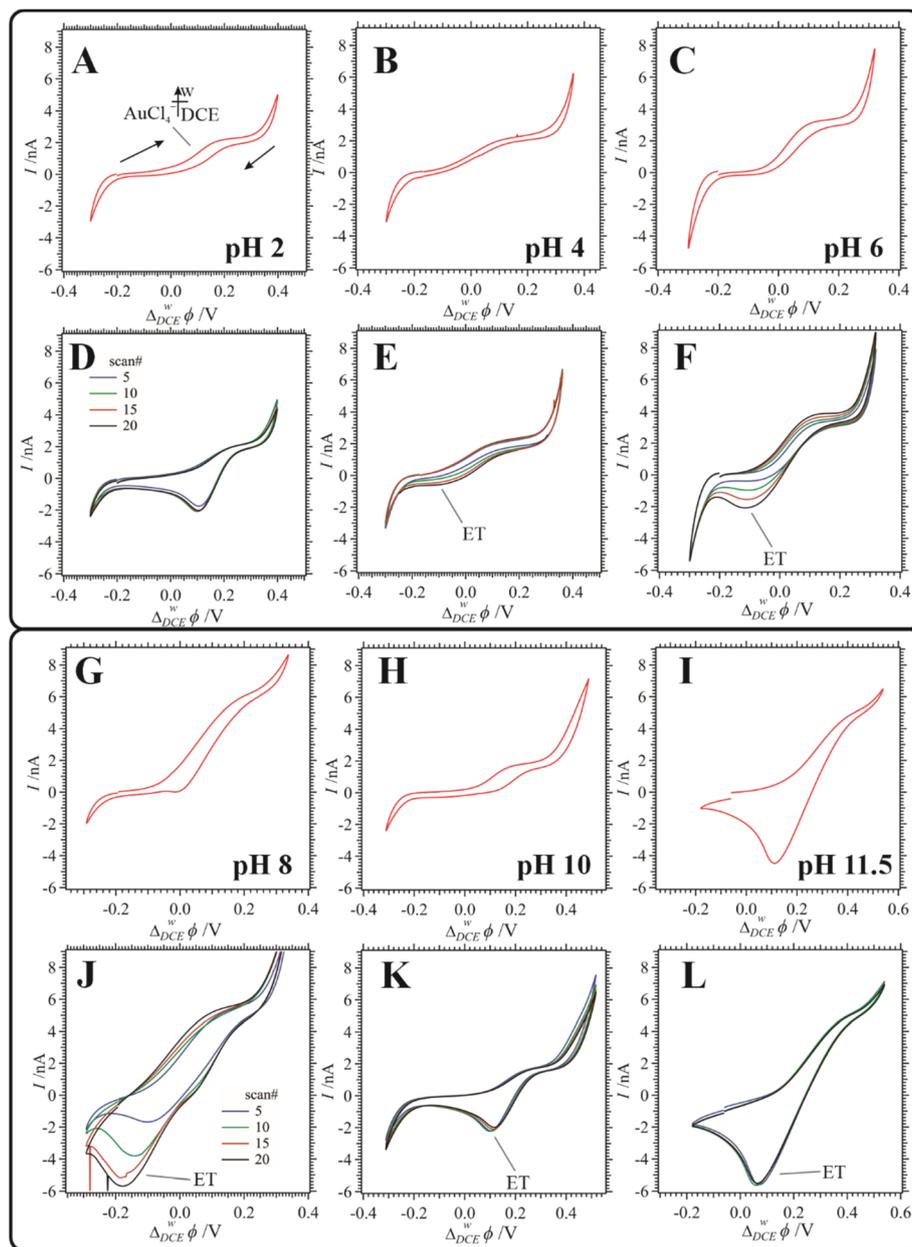
Fig. 2 CVs recorded using Cell 1 with 20 mM of DA(aq) and 1 mM $P_{66614}AuCl_4$(DCE) at a scan rate of 0.020 V s^{-1}; whereby, the pH of the aqueous phase as adjusted to pH 2, 4, 6, 8, 10, and 11.5 for panels A/D, B/E, C/F, G/J, H/K, and I/L, respectively. Panels A–C and G–I depict the first scan, while panels D–F and J–L show the 5th, 10th, 15th, and 20th scans as indicated inset. Solutions a pH $\geq$ 5 were purged with N_2 gas before use. Black arrows indicate scan direction. ET = electron transfer.
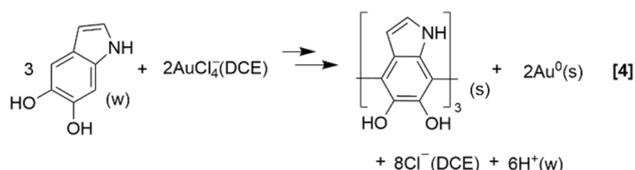
Scheme 4 Reaction [4] shows a proposed interfacial PDA formation reaction.

liberated Cl^- ions are either incorporated within the polymer matrix as a dopant or present at the surface of the formed Au NPs as a capping agent and do not undergo simple ion transfer from DCE $\rightarrow$ w – at least not at appreciable, detectable levels. It is also possible that $AuCl_4^-$ reacts with DA homogeneously within the aqueous phase, and the lack of a peak-shaped wave when scanning negatively is owing to an absence of $AuCl_4^-$ to transfer back.

At pH = 4 (Fig. 2B and E), a sigmoidal wave was again observed during both scan directions of the first cycle; however, unlike at pH 2, it retains its s-shaped profile even with repeated

CV cycling. The current intensity of the signal occurring during the scan from positive to negative potentials does increase subtly from 2.00 to 2.50 nA between the 1st and 20th scan. The CV profile at pH 6 undergoes a similar transition (Fig. 2F); however, by the 15th scan a peak-shaped wave has emerged at -0.11 V (Fig. 2J). Again, this is consistent with interfacial electron transfer from DA(aq) $\rightarrow$ AuCl$_4^-$(DCE) that is diffusion limited by DA(aq).

In 2015, Drye and Uehara's groups[50] characterized the Brust–Schiffrin mechanism of Au NP synthesis via AuCl$_4^-$ reduction at a w|DCE interface; whereby, they revealed the importance of the polymeric [Au(I)SR] species which is Au^{1+}-thiol species. This means that Au(III) was first reduced to Au(I). The presence of AuCl$_2^-$ or Au^{1+}-ligand coordinated species cannot be ruled out; however, XPS data (detailed below) seems to indicate the presence of only Au^{3+} and Au^0 species in the polymer film.

The sigmoidal waves during forward and reverse sweeps are present in the first CV scan up until pH 10, while the intensity of the peak current signal continues to increase with pH up to pH 11.5. At pH 11.5, the first CV already contains a peak-shaped wave during the initial scan from positive to negative potentials. These data suggest that the kinetics and thermodynamics of film formation improve concomitantly with increasing pH. As shown in Scheme 3, DA has 3 protonation/deprotonation steps;[46] moreover, polymerization of either the indole or catecholamine requires proton loss and is thus facilitated at more basic pHs. Examining the CVs shown in Fig. 2 altogether, it is likely that at pH 2 the kinetics of film formation are poor and improve concomitantly with increasing pH. Thus, these data agree with the generally accepted PDA formation mechanism and the need for a Brønsted base.[8,12,46,59,60]

After 25 CV cycles, a sample was ejected from the micropipette using the syringe incorporated into the back of the specialized holder and deposited onto a GCE and carefully rinsed to remove any residual, unreacted material. The modified GCE surface was then imaged using SEM; whereby, the images captured of films formed at pH equal to 4, 8, 10, and

11.5 have been given in Fig. 3A–D, respectively. These images demonstrate that the Au NP incorporated PDA nanocomposite are formed via the w|DCE interfacial reaction depicted in Scheme 1. Because the nanocomposite was ejected out of the pipette tip, it is likely that the side facing up in the SEM images (see also Fig. S1 of the SI) is the aqueous side of the film. Polymer films generated at the ITIES have been shown to have Janus-type[34,35,61] properties since they grow differently on either side of the interface. Nishi et al.[61] demonstrated that Au NP/polythiophene films generated at a water|ionic liquid (w|IL) interface demonstrated long polymer strands on the IL side containing the hydrophobic monomer, while Au NP growth continued on the water side which contained the KAuCl$_4$ hydrophilic salt. Any AuCl$_4^-$ that partitioned from w to IL formed Au nanofibers. Similarly, Scanlon's group[34,35] electrogenerated poly(3,4-ethylenedioxythiophene) (PEDOT) films at a large w|TFT interface; whereby, a cerium sulfate salt in the aqueous phase acted as the electron acceptor while EDOT was dissolved in the TFT phase and behaved as the electron donor. In that case, the aqueous side was very smooth, while the oil side was rough due to the continued polymer growth. Because the micro-ITIES was employed herein, it was not possible to flip the film over and image the portion of the film formed on the DCE side of the ITIES. Based on these previous reports, it is expected that there would be morphological differences between the aqueous and oil sides of the nanocomposite. The film generated at pH 4 had more prominent Au NPs across its surface (Fig. 3A) and was revealed by EDX mapping (Fig. S1). However, at higher pHs the film was much thicker, and these NPs were difficult to observe and likely encapsulated within the polymer matrix. Fig. S2 of the SI shows EDX mapping images of the modified GCE surface for Au and O distributions. At low pH, Au is distributed evenly; however, as the pH increases Au seems to be pushed outwards forming a ring towards the outside edge of the GCE disc. This may be owing to Au NP encapsulation; whereby, they cannot be detected by EDX. However, at this stage, it is still poorly understood and will be the focus of future investigations. All Au NP/PDA films were electrogenerated using only 1 series of 25 CVs at a micro-ITIES (25 μm in diameter) as depicted in Fig. 2 before being deposited onto the GCE; nevertheless, the nanocomposite did spread to cover all the GCE surface (4 mm diameter). The film coverage of the GCE can be seen in the SEM images presented in Fig. S2A–C. When films were deposited, they were gently rinsed with MilliQ water to remove any excess supporting electrolyte or unreacted starting material. The fragile, soft nature of the film may explain how this coverage was achieved. It may also indicate that the Au NPs are only loosely bound with the polymer matrix; thus, the concentration of Au NPs towards the outer edge of the GCE disc may be a 'coffee-ring' effect and a result of ejecting the film onto the solid electrode surface from the micropipette. Another possible reason for Au NP concentration towards the outside ring of the film could be due to hemispherical diffusion of AuCl$_4^-$ towards the w|DCE interface. This would result in the outer edge of the micropipette-supported ITIES receiving a higher flux of AuCl$_4^-$ to the outside rim of the interface relative to its centre possibly generating a higher number of Au NPs
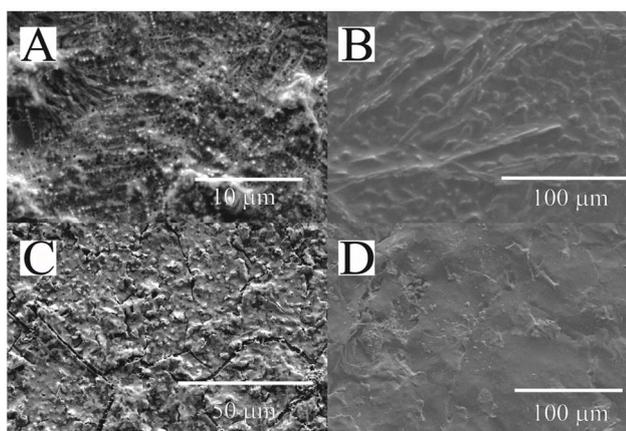

Fig. 3 Scanning electron microscopy (SEM) images of Au NP/poly(DA) films deposited onto glassy-carbon electrodes (GCE). Films were generated as described in Fig. 2 with the aqueous pH adjusted to (A) 4, (B) 8, (C) 10, and (D) 11.5.

in this region. This higher flux is often observed at ultra-microelectrodes;[62] thus, these data would agree with those reports.

Electrogenerated Au NP/PDA films were also deposited onto ultra-thin lacey carbon Au TEM grids and imaged. Fig. 4A, C and E depict the TEM micrographs captured of films formed at pH 4, 8, and 10, respectively. The Au NPs were sized using ImageJ software and Fig. 4B, D and F show the respective histograms compiled (green, bar plots) as well as the Gaussian curve fitting (red traces) performed using Igor Pro (version 9). NPs were measured to be 25 ± 12, 5.8 ± 1.7, and 15.2 ± 2.4 nm for nanocomposites formed at pH's of 4, 8, and 10, respectively. The error in the NP sizing was taken from the half-width-at-half-height from the Gaussian fitting. The Au NPs within the nanocomposite film generated at pH 4 (Fig. 4A and B) were observed inside spherical dark spots on the TEM grid which are hypothesized to be the polymer matrix. At pH 8 (Fig. 4C and D), NPs are well distributed within the polymer film which seemed to cover the TEM grid. Finally, at pH 10 (Fig. 4E and F) polymer
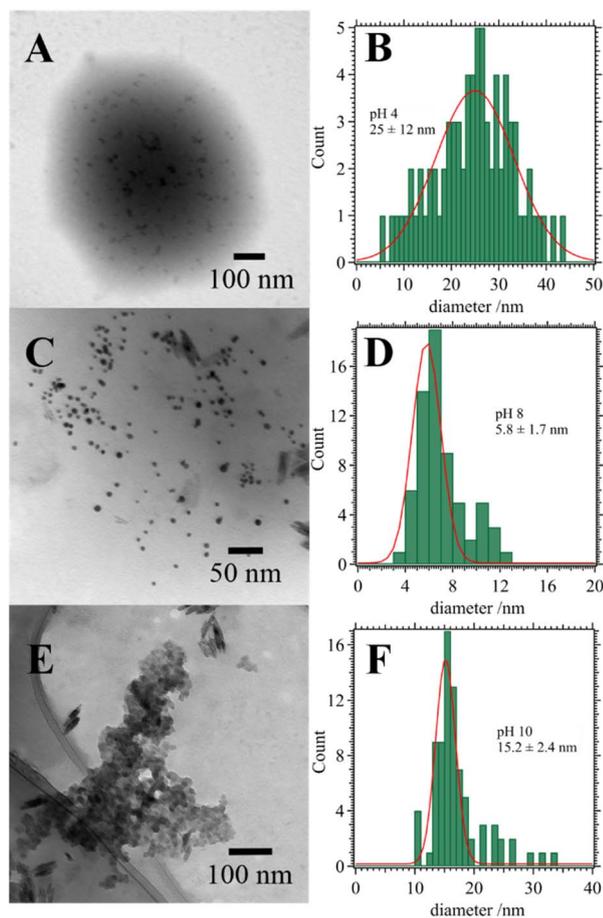

Fig. 4 TEM images (A, C and E) taken of Au NP/poly(DA) films formed as described in Fig. 2 and deposited on TEM grids with the aqueous pH at 4 (A and B), 8 (C and D), and 10 (E and F). (B, D and F) Histograms of Au NP diameters measured using ImageJ software of the accompanying image. The red, solid trace shows the Gaussian curve fitting. Inset are the Gaussian peak maximums plus/minus the half-width-at-half-height.
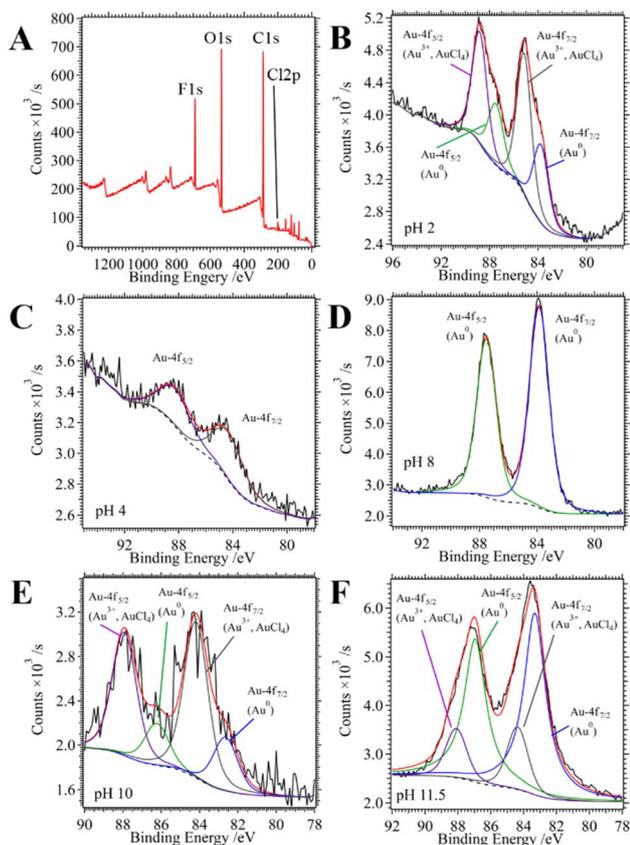
nanocrystals/needles where also observed within the nanocomposite and Au NPs where not as evenly distributed as observed at lower pH's. At low pH, the film was much thinner and more fragile making it difficult to manipulate by hand. The trend in Au NP size is surprising. Since the electropolymerization kinetics are likely slow at low pH our initial hypothesis was that Au NP size would increase with increasing pH; however, this was not the case. It likely means that the interplay between Au NP formation and PDA polymerization is much more complex and in need of further investigation.

Combining the voltammetric as well as SEM and TEM image observations, it is likely that the kinetics of film formation are slow at lower aqueous pH and increase concomitantly with alkalinity. At lower pH, the Au NPs are more exposed on the surface, while as the pH increases, they become occluded by the polymer matrix. As described above, this agrees well with earlier investigations of PDA formation.[12,60] Indeed, alkaline aqueous phases are often exploited to spontaneously generate PDA which can be dip-coated onto surfaces for anti-corrosion or electrochemical applications.[46,59] These results also agree with the electropolymerization of thiophene-containing monomers at the ITIES.[34,35,39–41,43] Our group recently demonstrated that the aqueous pH could be exploited as a means to control the electropolymerization of 2,2′:5′,2″-terthiophene (TT).[43] Exchanging DCE for another solvent, e.g., TFT, or an IL, e.g., tetraoctylphosphonium tetrakis(pentafluorophenyl)borate ($P_{8888}TB$), can be used to alter the nanocomposite morphology of Au NP/poly(9-vinylcarbazole).[39] Both TT and 9-vinylcarbazole polymerization rely on a deprotonation step to form a conducting polymer similar to PDA formation. Nevertheless, these data show that the aqueous phase pH plays a key role in electropolymerization thermodynamics and kinetics.

XPS spectra were also collected for the films generated at each pH regime. Au NP/PDA films were deposited onto Al foil and then rinsed with MilliQ water before acquisition of the spectra. Fig. 5A depicts the XPS survey spectra obtained using the Au NP/PDA film electrogenerated at pH 2. The F-1s, O-1s, and C-1s signals are present at roughly 690, 534, and 287 eV, respectively. F-1s was only observed in films generated at pH's 2, 6, and 8. This may indicate that $B(C_6F_5)^-$ is acting as a dopant in the likely p-type PDA matrix. O-1s, N-1s, and C-1s signals were present in all spectra (see also Fig. S6 of the SI).

Fig. 5B–F show high-resolution XPS spectra for films generated at pH 2, 4, 8, 10, and 11.5, respectively, within the binding energy domain expected for Au-4f. The Au^0 $4f_{7/2}$ and $4f_{5/2}$ orbitals are expected to appear at roughly 83.8 and 87.5 eV, respectively.[63–66] Multi-peak fitting reveals two additional peaks at 84.4 and 88.1 eV slightly positively shifted relative to those for Au^0 which are likely Au^{3+} or $AuCl_4^-$.[67] Thus, either some unreacted $AuCl_4^-$ salt remains, or Au^{3+} species have coordinated to the catechol moiety of DA or the PDA backbone. While the sample was rinsed prior to XPS analysis, residual $P_{66614}AuCl_4$ from the DCE phase may be possible. The XPS spectra collected from the film formed at pH 6 showed no detectable Au-4f signal (data not shown). It is possible that Au NPs/$P_{66614}AuCl_4$ salt was dislodged during sampling and rinsing; however, it may be that Au NPs were not incorporated

Fig. 5 X-ray photoelectron spectroscopy (XPS) spectra recorded using Au NP/PDA films. (A) XPS survey for film generated at pH 2. (B–F) High-resolution spectra targeting Au-4f for films generated at pH 2, 4, 8, 10, and 11.5, respectively. Experimental traces are shown in black, while the red, purple, green, and blue curves depict the multi-peak fitting for the Au-$4f_{5/2}$ and Au-$4f_{7/2}$ spin orbital splitting peaks, as indicated inset. The red trace is the compiled fitting envelope, while the dashed, black curve was the calculated background trace.

into the film. Because Au NPs were evidenced using TEM and SEM, including EDX mapping (see Fig. S2), the former is the more likely scenario.

Fig. S6C shows high-resolution XPS spectra collected in the Cl-2p region. Cl-$2p_{3/2}$ has organic character towards 200 eV and metallic when shifted to 198.5–199 eV (red vertical bar in Fig. S6C).[68] Interestingly, Cl-2p is present at all pH's and gains metallic character with increasing pH, i.e., signal shifts towards 198.5 eV. At low pH, Cl$^-$ is acting as a dopant, while as the pH increases and the kinetics of polymerization improve, likely more $P_{66614}AuCl_4$ salt is incorporated into the polymer matrix. Nevertheless, Au^0 signal is still strong in these pH regions, so Au NPs are still present. A signal for P-2s can also be seen in some pH's which may indicate the presence of the P_{8888}^+ (tetra-octylphosphonium) or P_{66614}^+ (trihexyltetradecylphosphonium) cation from the DCE supporting electrolyte or $P_{66614}AuCl_4$ IL.

Water contact angle (WCA) measurements (data not shown) demonstrated that the film was very hydrophilic. Indeed, a 2 µL water droplet deposited on the surface of films electrogenerated

at any pH spread so rapidly it could not be captured in a single photo by the CCD camera.

Au NP/PDA samples were also collected and analysed using FTIR and compared with DA, see Fig. S7. The peak at 3338 cm^{-1} which is associated with –NH$_2$ stretch and disappears after electropolymerization. Meanwhile, the peak shift from 1618 to 1598 cm^{-1} from DA to PDA is likely a result of the formation of the π-conjugated indole. Thus, it is likely DA is forming PDA but first undergoes intramolecular cyclization to form DHI.

A series of shake-flask experiments at increasing pH were performed in 20 mL scintillation vials using 20 mM DA(aq) and 1 mM $P_{66614}AuCl_4$(DCE); whereby, both phases were purged with N$_2$ gas for ∼30 min before being combined, sealed, shaken, then left to stand for 24 hours. Fig. 6A depicts photographs taken afterwards, while Fig. 6B and C show UV/Vis spectra recorded of the aqueous phase before and after 24 hours, respectively. At pH 2 and 4, there is no observable formation of black PDA, while at pH 6 a slight reddish hue can be seen in the aqueous phase. This likely points to AuCl$_4^-$ spontaneous ion transfer followed by homogeneous reaction with DA generating Au NPs. pH's 8–11.5 show increasing amounts of a black precipitate, likely PDA. Within the UV/Vis spectra before interfacing the aqueous and DCE phases there is a peak at roughly 280 nm that shifts to 300 nm as the pH increases. Additionally, a signal grows at ∼435 nm. These are consistent with π–π* electronic transitions owing to the presence of the aromatic ring with the catechol moiety and agree well with the work of Sanchez-Rivera et al.[47] After the two phases are combined and mixed for 24 hours (Fig. 6C), the signals at 280 and 435 nm broaden and there appears to be a shoulder above 435 nm at pH 10 and 11.5 that may indicate the presence of the Au NP localized-surface-plasmon-band (LSPR) which should appear at
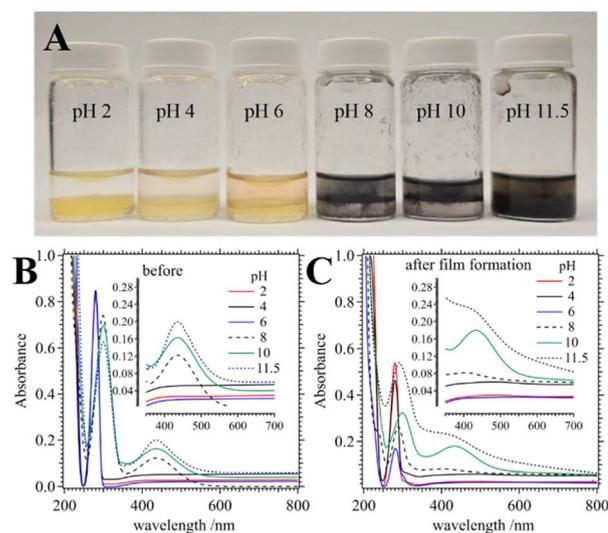

Fig. 6 (A) Photographs of shake-flask experiments after 24 hours with the aqueous phase adjusted to the pH indicated inset. The aqueous phase contained 20 mM DA while the DCE phase contained 1 mM of $P_{66614}AuCl_4$. Both phases were purged with N$_2$ gas prior to mixing for ∼30 min. (B) and (C) depict UV/Vis spectra recorded of the aqueous phase before and after, respectively, mixing and waiting 24 hours at the aqueous pH shown inset.

roughly 520 nm.[69] These data also agree with the thermodynamic calculations surrounding Scheme 4 discussed below.

Using scanning electrochemical microscopy (SECM), probe-approach-curves (PACs) were measured towards a Au coated Si wafer modified with Au NP/PDA nanocomposite electro-generated at a micro-ITIES at increasing pH in a solution of 0.9 mM ferrocene methanol (FcCH$_2$OH) as redox mediator, 0.1 M phosphate buffer solution (PBS), and 0.1 M KCl (see Fig. 7) as well as using a carbon fibre UME. The UME was fabricated using 7 μm diameter carbon fibre and its ratio of outer glass radius (r_g) to electroactive inlaid disc radius (r_a), or R_g was confirmed to be ∼7 by comparing it to a simulated PAC of an insulating substrate (experimental: dashed, black trace and simulated: ○ marker curve in Fig. 7). Simulated PACs were generated using Comsol Multiphysics (version 6.3) as described in detail elsewhere.[39] PACs were performed by biasing the UME at potential within the steady state oxidation current (i_{ss}) of FcCH$_2$OH. PACs have been plotted using the normalized current (i/i_{ss}) and tip-to-substrate distance ($L = d/r_a$); whereby, d is the actual tip-to-substrate distance.

The rate of the redox mediator re-reduction at the substrate surface (k) decreased concomitantly with increasing pH. For example, at pH = 2 or 4, the simulated curve with $k = 3.4 \times 10^{-3}$ cm s^{-1} showed the best overlap, while $k = 1.25 \times 10^{-3}$ cm s^{-1} generated the simulated PAC with the best overlap for the film generated at pH 11.5. The decrease in k as pH increases likely points to decreased conductivity of the film.

Au NP/PDA composites deposited on GCEs and carefully rinsed were then investigated as sensors for DA detection in a 0.1 M phosphate buffer solution (PBS). These experiments were performed in 3-electrode mode using a Pt mesh counter
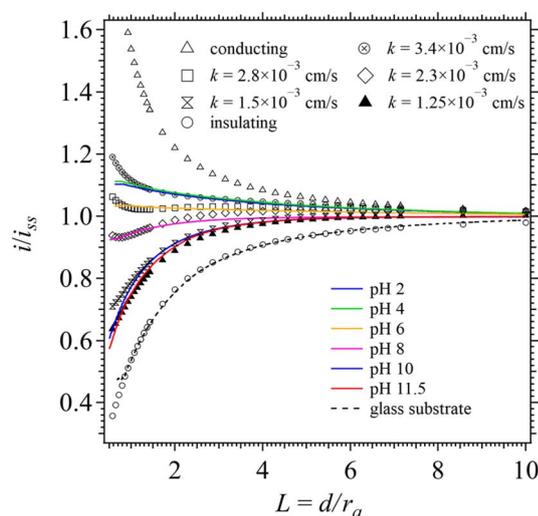
(CE) and an Ag/AgCl reference electrode (RE). All solid/electrolyte potentials have been plotted *versus* Ag/AgCl unless otherwise indicated. Fig. 8A shows CVs recorded at 0.050 V s^{-1}; whereby, the red, solid and dashed curves were recorded using a bare GCE with and without 0.5 mM DA, respectively. Next, an Au NP/PDA film electrogenerated at pH 4 using Cell 1 with 20 mM of DA in the aqueous phase and 25 CV cycles was used to measure the black, dotted trace. Finally, the same nanocomposite film modified GCE was employed to record a CV with
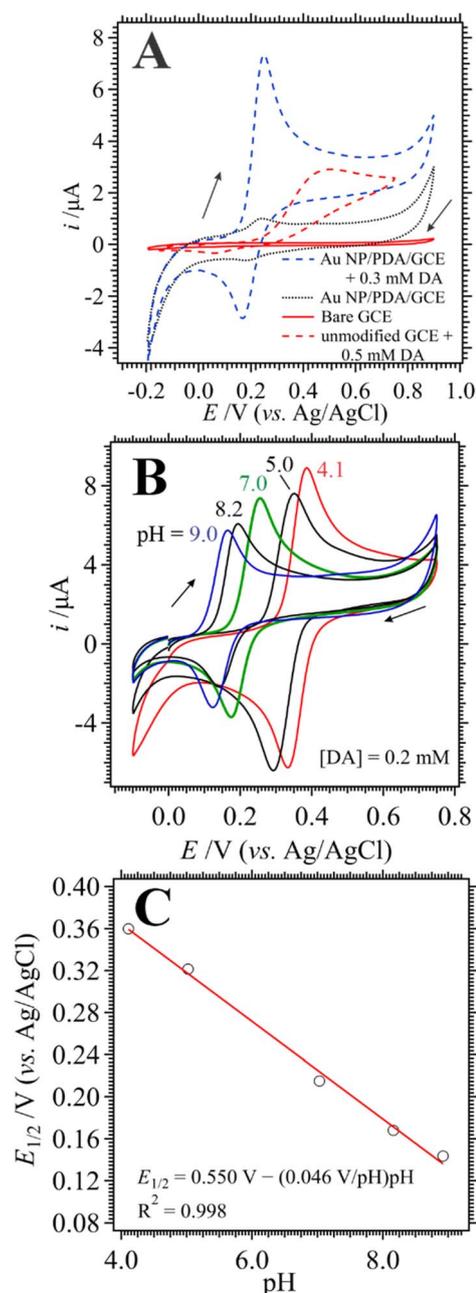

Fig. 8 (A) CVs recorded at a bare and Au NP/PDA modified GCEs at 0.050 V s^{-1} in a 0.1 M phosphate buffer solution (PBS) with [DA], as well as when changing the pH indicated inset (B). Black arrows indicate scan direction. (C) Plot of $E_{1/2}$ *vs.* pH as obtained from DA redox peaks in B.

Fig. 7 Probe approach curves (PACs) recorded using a carbon fibre ultramicroelectrode (UME), r_a = 3.5 μm and an $R_g \approx 7$, towards Au coated Si wafers modified with Au NP/PDA composites electro-generated at the pH indicated inset (line traces). The UME was moved at a rate of 0.5 μm s^{-1}. Overlaid are simulated PACs using generated using Comsol Multiphysics software at the substrate rate constant (k) indicated inset. Comsol code has been described in detail previously by us.[39]

0.3 mM of DA added to the electrolyte solution (blue, dashed plot). The CV obtained at the bare GCE without DA added is featureless in both forward and reverse scans with a modest capacitive current of ~60 nA. With DA added, the bare GCE contains an irreversible electron transfer signal for DA oxidation with a peak potential (E_p) at ~0.5 V.

After modification with the nanocomposite, a redox couple was observed with a half-wave potential ($E_{1/2}$) at 0.208 V (*vs.* Ag/AgCl) and a peak-to-peak separation (ΔE) of ~0.058 V. This is likely the oxidation/reduction of residual, unreacted DA within the nanocomposite. However, this signal persists even after several CV cycles; thus, the black, dotted curve in Fig. 8A is considered at a steady state condition. The narrow ΔE indicates that the heterogeneous electron transfer of DA across the nanocomposite/electrolyte interface is at least quasi-reversible for a 2-electron transfer as described by reaction 2 (Scheme 3). This assumes the criteria for reversibility is $\Delta E \approx 0.057$ V n^{-1}, where n is the number of electrons transferred.[54,70] If 0.3 mM of DA is added to the solution (blue, dashed curve), then the signal at $E_{1/2} = 0.208$ V increases with a final anodic peak current ($i_{p,a}$) of 7.05×10^{-6} A. ΔE increased as well to 0.078 V, while the ratio of $i_{p,a}$ to the cathodic peak current ($i_{p,c}$), $i_{p,a}/i_{p,c}$ was ~1.56. This slight increase in ΔE may be owing to a modest resistivity in the conductive nanocomposite film or uncompensated solution resistance, *i.e.*, *iR*-drop. Nevertheless, this highlights the good electron transfer reactivity of the nanocomposite modified GCE electrode and it's significant improvement *versus* the bare GCE in DA oxidation performance. While the oxidation potential of DA is pH dependent,[71] $E_{1/2}$ is in good agreement with previous reports.[71,72] One can also intuit that the conductivity of the film is quite good.

Fig. 8B depicts i–E curves measured under similar conditions with [DA] = 0.2 mM while changing the pH. $E_{1/2}$ for the DA redox signal shifts towards negative potentials as the pH increases from 4.1 to 9.0. This demonstrates the enhanced thermodynamic driving force of DA oxidation with increasing pH. A plot of $E_{1/2}$ *vs.* pH is presented in Fig. 8C while a linear regression fitting is shown as the solid, red trace; the linear fitting equation is provided inset. This trend can be used to calculate the thermodynamics of electropolymerization at the liquid|liquid interface as well. Fig. S3A and B of the SI show the trends in $i_{p,a}$, $i_{p,c}$, $i_{p,a}/i_{p,c}$ and ΔE with changing pH. There is a slight decrease in $i_{p,a}$ and $i_{p,c}$ with increasing pH, while their ratio remains fairly close to ~1.0. Simultaneously, ΔE shows a sharp increase at pH 7; however, at the other pH's it is less than 0.06 V and drops as low as 0.043 V at pH 9.0. Thus, it is likely that DA oxidation is at least quasi-reversible at the Au NP/PDA modified electrode.

The Ag/AgCl RE employed has an operational range from roughly pH 6 to 11.[73] While the pH 4.1 and 5.0 experiments may be outside this region, the Ag/AgCl RE has been employed for convenience and the error in $E_{1/2}$ is likely small.

Using the pH dependence shown in Fig. 8C, which is in good agreement with previous reports,[74,75] one can establish the standard redox potential of DA, $E_{DA^+/DA}^{o,H_2O}$ (*versus* SHE), such that it can be described by,

$$E_{DA^+/DA}^{o,H_2O} \approx 0.75 \text{ V} - (0.046 \text{ V/pH})\text{pH} \qquad (1)$$

whereby, -0.046 V-per-pH is the slope of the pH dependence as given in Fig. 8C. If the ratio of electrons transferred to protons lost is 1 : 1, then this slope should be -0.059 V-per-pH. It is interesting, however, that in multiple reported cases, including this one, it was found to be close to that shown in eqn (1).[74,75]

$AuCl_4^-$ is a strong oxidizing agent with a standard reduction potential in water, $E_{Au(III)/Au}^{o,H_2O} = 1.002$ V;[76] however, this is shifted far more negatively in organic solvents.[77,78] To establish the redox potential of $AuCl_4^-$ in DCE, $AuCl_4^-/Au^0$ was measured in the DCE phase using a carbon fiber UME, $r = 3.5$ μm, while referencing the potential *versus* the ferrocene (Fc) redox couple, assuming $E_{Fc^+/Fc}^{o,DCE} = 0.640$ V.[79,80] CVs were measured in solutions containing 5 mM of $P_{8888}TB$ as supporting electrolyte as well as 1 mM of either Fc or $P_{66614}AuCl_4$ and are provided in Fig. S4A and B, respectively, of the SI. A solution of 1 mM Fc and $P_{66614}AuCl_4$ plus supporting electrolyte was mixed in DCE resulting in the generation of a purple Au NP suspension. Fc has been shown to react with gold salts donating electrons and spontaneously generating Au NPs with ferrocenium (Fc$^+$) acting as the capping agent.[44,81] Nevertheless, voltammetric response measurements in this mixture (Fig. S4C of the SI) show that residual $AuCl_4^-$ and Fc are present even after they are allowed to react for 5–10 min. This was sufficient to estimate $E_{Au(III)/Au}^{o,DCE}$ as -0.920 V. A steady-state response was also observed for what is believed to be, $AuCl_4^- + 2e^- \rightarrow AuCl_2^- + 2Cl^-$, with $E_{Au(III)/Au(I)}^{o,DCE}$ calculated to be -0.20 V. These values are in good agreement with those measured and calculated from first principles at a microelectrode by Gründer *et al.*[77] of $E_{Au(III)/Au}^{o,DCE} = -0.9$ V and $E_{Au(III)/Au(I)}^{o,DCE} = -0.27$ V, respectively.

With these values in hand, the thermodynamics of the heterogeneous liquid|liquid electron transfer reaction including the interfacial electron transfer potential ($\Delta_{DCE}^w\phi_{ET}$) were calculated for the first step in the polymerization reaction if one assumes that the stoichiometric ratio of $AuCl_4^-$ to DA is 2 : 3, through following formula,[44,80]

$$\Delta_o^w\phi_{ET} \approx E_{DA^{2+}/DA}^{o',H_2O} - E_{Au(III)/Au}^{o',DCE} - \frac{RT}{F}(\ln 10)\text{pH} \qquad (2)$$

$\Delta_{DCE}^w\phi_{ET}$ was calculated to vary from 1.5 to 0.5 V moving from pH 2 to 11. In this way, the interfacial electron transfer reaction is not spontaneous ($\Delta G > 0$) and polarization is required to achieved electropolymerization. It is likely that nucleation sites along the glass rim of the pulled borosilicate glass capillary establishing the micro-ITIES improve the thermodynamics lowering the driving force of the reaction and enhancing the overall electropolymerization. This would shift the potential more positively as the pH increased into the observable PPW.[39-41] DA demonstrated very poor solubility in DCE; thus, it is unlikely that DA transfers and undergoes homogeneous reaction with $AuCl_4^-$ in the DCE.

Considering an alternative mechanism, whereby $AuCl_4^-$ partitions and undergoes homogeneous electron transfer with DA in the aqueous phase, then an alternate equation is needed as shown below,

$$E_{cell} \approx E_{Au(III)/Au}^{o',H_2O} - E_{DA^{2+}/DA}^{o',H_2O} + \frac{RT}{F}(\ln 10)pH \qquad (3)$$

Using eqn (3), large negative ΔG values are calculated indicating a spontaneous reaction pathway that may be a driving force for $AuCl_4^-$ transfer to water. This would manifest as a relatively large positive current offset that was not observed; therefore, it is likely the small interfacial size limits this reaction pathway. The shake-flask experiments shown in Fig. 6A at a large ITIES also demonstrate that $AuCl_4^-$ transfer followed by homogeneous reaction in the water phase is not favoured at low pH; however, it may be a factor as pH increases.

Fig. S5A depicts the i–E curves recorded at an Au NP/PDA modified GCE while changing the scan rate, while Fig. S5B contains plots of $i_{p,a}$ and $i_{p,c}$ versus $v^{1/2}$. Linear curve fittings of the latter show good correlation with R^2 values of ~0.999. The number of electrons transferred (n) was calculated using the Randles-Ševčík equation[70,82] (eqn (4)) and assuming a DA diffusion coefficient (D) equal to 0.54×10^{-5} cm^2 s^{-1} as described by Corona-Avendaño et al.[83]

$$i_p = 0.4463\left(\frac{F^3}{RT}\right)^{1/2} n^{3/2}AD^{1/2}c^*v^{1/2} \qquad (4)$$

In this way, $n \approx 1.87$ and 2.00 were calculated for $i_{p,a}$ and $i_{p,c}$ versus $v^{1/2}$, respectively. This agrees well with the 2-electron DA oxidation generally to DAQ (Scheme 3). The redox chemistry of DA has been studied extensively at the GCE/electrolyte interface.[83] Zhang and Dryhurst[84] investigated DA electrochemistry at a pyrolytic graphite electrode that showed reversible DA oxidation. They also identified several intermediate species using HPLC and proposed that DA is oxidized to DAQ which can then undergo the intramolecular cyclization to form I56D or DHI (see Scheme 3). DHI has a much lower oxidation potential than DA[84] and thus, readily polymerizes to form PDA and melanin.
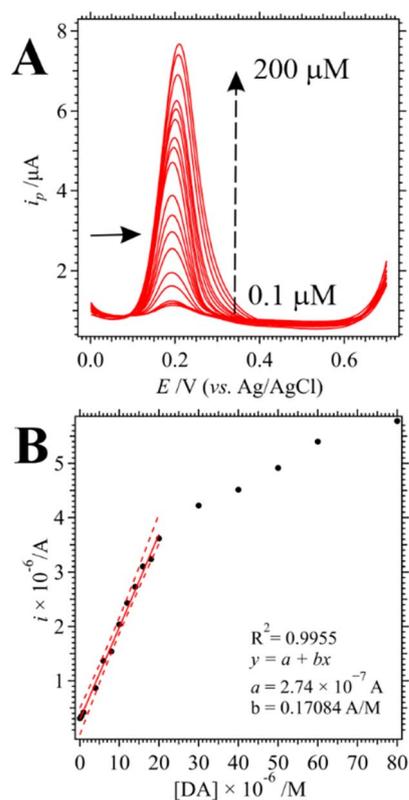

Fig. 9 (A) Differential pulse voltammograms (DPVs) recorded at a Au NP/PDA modified GCE electrode in 0.1 M PBS. (Film formation parameters). DPV was performed with a pulse amplitude, width, period, and increment of 0.07 V, 0.050 s, 0.2 s, 0.001 V, respectively. (B) Plot of i_p versus [DA] obtained from A. Experimental i_p values are plotted as solid circles (●) while linear regression curves are solid, red traces. The linear regression equation and its associated R^2 value is given inset along with the equation of the line-of-best-fit (LOBF). Dashed, red curves are the LOBF positive and negative as described in the SI section 4.
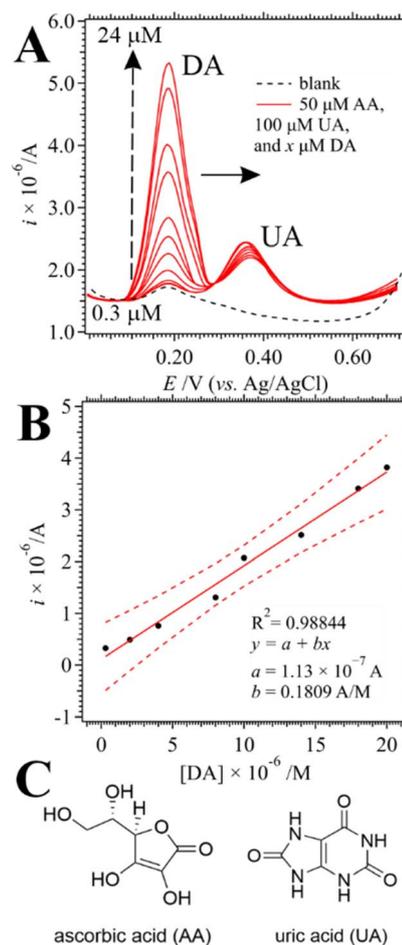

Fig. 10 (A) DPVs recorded under the same conditions as Fig. 9A, however, with different concentrations of DA, AA, and UA added, as indicated inset, as interferents. DA and UA oxidation waves are labelled inset. (B) Calibration curve constructed using the i_p data from A. Red trace is the linear curve fitting while the red, dashed traces are lines-of-best-fit at a 99.9% confidence interval as described in Section 4 of the SI. Linear regression equation and R^2 values are written inset. (C) Chemical structures of ascorbic and uric acid.

Table 1 Select contemporary reports of electrochemical dopamine sensors. GO = graphene oxide; rGV = reduced graphene oxide

Electrode functionalization material	Technique	c_m μM^{-1}	Linear range μM^{-1}	Ref.
Laccase-carbon dots	DPV	0.08	0.25–76.81	89
PEDOT–GO–polyphenol oxidase	Amperometry	8×10^{-9}	$5 \times 10^{-5} - 0.35$	90
Au NPs + polymelamine	DPV	0.067	0.1–11	91
rGO-Fe$_3$O$_4$/AgNPs	DPV	0.004	0.015–100	92
FeMoSe$_2$–GO	DPV	0.002	0.04–40	93
Au NP/PDA–GCE	DPV	0.27	0.1–24	This work

Fig. 9A shows differential pulse voltammograms (DPVs) measured in 3-electrode mode using Au NP/PDA modified GCEs while changing [DA]. Fig. 9B depicts the calibration curve generated using the peak current values for DA oxidation from Fig. 9A. The Au NP/PDA film was electrogenerated using Cell 1 at pH 4.1, 20 mM of DA, and 25 CV cycles. This pH was chosen as the Au NPs appeared more visually exposed in the SEM images. Other film generation conditions were investigated; however, these are showcased here as a proof-of-concept. The i_p versus [DA] plot has a linear region spanning roughly between 0.1–20 μM; afterwards, the curve deviates.

Next, the influence of interferents such as AA and UA were investigated using a 0.1 M PBS buffer solution containing 0.1 M KCl electrolyte at pH 5.5–6 (see Fig. 10A). Even with no DA added, a DA oxidation wave was observed at 0.17 V like that seen using cyclic voltammetry (see dashed, black trace in Fig. 8A). No peak for AA was observed even at concentrations of 50 or 100 μM (data not shown), and its oxidation may be inhibited at the modified electrode interface. A UA oxidation peak was observed with a peak potential of ∼0.37 V. As [DA] increased from 0.3 to 24 μM, the UA anodic peak current decreased. Simultaneously, the UA peak potential shifts slightly by ∼0.016 V; however, at higher [DA] it stabilizes. This may be owing to the Ag/AgCl reference electrode, which is on the lower end of its operational range,[73] or it may be caused by DA inhibiting UA oxidation. Nevertheless, using these DA peak signals a new calibration curve was constructed with both AA and UA interferents present (see Fig. 10B). There is a sharp decrease in the slope of the linear correlation curve which indicates a loss in sensitivity. The R^2 value is still high at 0.979 showing a good fitting.

A limit-of-detection (c_m) was calculated using the average of 3 blank DPV signal profiles and the following two equations,[85]

$$S_m = \bar{S}_{blk} + k_m \sigma_{blk} \quad (5)$$

$$c_m = \frac{S_m - \bar{S}_{blk}}{m} \quad (6)$$

Whereby, $\bar{S}_{blk}$ is the mean blank signal, σ_{blk} is the standard deviation of the blank signal, k_m is the variation in the blank, and m is the slope of the calibration curve. Using a k_m value of 3, c_m was determined to be 0.27 and 0.43 μM for the calibration curves shown in Fig. 9B and 10B, respectively. Thus, there is a slight loss in sensitivity when AA and UA are present. The Au NP/PDA modified electrode is an order of magnitude less sensitive than some of the highest sensitivity platforms

reported.[86,87] However, these platforms often rely on complex enzyme- or antibody-based modifications that are challenging to achieve,[87] or are not practical for *in vivo* implementation. Karim *et al.*[88] recently wrote a comprehensive review of dopamine electrochemical sensors. Table 1 provides a few select electrode modifications for comparison with the work presented herein.

Thus, this proof-of-concept electrochemical sensing device, with the potential of generating a free-standing, conductive PDA electrode is promising and comparable to other biosenors in the field in terms of c_m and limit-of-linearity (see Table 1).

Conclusions

In summary, Au NP incorporated PDA films were electro-generated at a micro liquid|liquid interface (25 μm in diameter) under external, potential control. DA was dissolved in the aqueous phase, while a $P_{66614}AuCl_4$ ionic liquid was added to the DCE phase. The influence of aqueous pH on film formation was observed voltammetrically which manifested as a more prominent heterogeneous electron transfer wave as pH increased. Moreover, the film morphology was shown to change using SEM imaging. At low pH, the film seemed thinner with the Au NPs more exposed on the surface; however, as the pH was adjusted to become more alkaline the film thickness seemed to increase and NPs were more encapsulated. The ease of film formation at higher pH's agreed with thermodynamic calculations and previous DA as well as PDA studies.[8,12,46,59,60] The need for a Brønsted base to enhance the thermodynamics of electropolymerization also agreed with other liquid|liquid electrochemical reports.[34,35,39–41,43,48]

Au NP/PDA films deposited onto a large (mm scale) GCEs were then used as a proof-of-concept platform for DA detection with and without the presence of interfering species such as AA and UA. DA oxidation was shown to be quasi-reversible with ΔE varying from roughly 0.04–0.08 V with increasing pH; simultaneously, the pH dependence of $E^{o,H_2O}_{DA^+/DA}$ was found to agree quite well with previous reports.[74,75] A good linear dynamic range was discovered for DA detection using the Au NP/PDA modified GCE from 0.2 to 20 μM. Moreover, the limit-of-detection (LOD) was quantified with and without the addition of other biomolecules that act as interferents, specifically AA and UA. The LOD changed slightly from 0.27 to 0.43 μM; thus, there was a modest decrease in the overall sensitivity of the biosensor. Future investigations will include modifying microelectrodes as well as using the Au NP/PDA composite as a free-standing electrode. The latter proved challenging in the present work as the film

was quite fragile. While this may be disadvantageous for an *in vitro* biosensor device, the nanocomposite materials softness may prove to be quite advantageous for bioimplantation and avoiding rejection by the host.

The liquid|liquid interface is often employed as an analogue or approximation of the biological membranes. This work showcases how it can be exploited to generate complex nanocomposites as well as large biomolecules such as PDA. We hope this work will be a potential springboard for novel studies of nature's approach to molecular synthesis based on the ITIES.

Author contributions

L. N.: formal analysis; data curation; formal analysis; investigation; writing – review & editing. F. K.: analysis; data curation; formal analysis; investigation; E. B. E.: conceptualization; funding acquisition; supervision; methodology; project administration; formal analysis; T. J. S.: conceptualization; funding acquisition; supervision; methodology; project administration; formal analysis; writing – original draft; writing – review & editing.

Conflicts of interest

There are no conflicts to declare.

Data availability

Acknowledgements

Notes and references

1 R. Franco, I. Reyes-Resina and G. Navarro, *Biomedicines*, 2021, **9**, 109.

2 I.-E. Pralea, R.-C. Moldovan, A.-M. Petrache, M. Ilieș, S.-C. Heghes, I. Ielciu, R. Nicoară, M. Moldovan, M. Ene, M. Radu, A. Uifălean and C.-A. Iuga, *Int. J. Mol. Sci.*, 2019, **20**, 3943.

3 T. Ligonzo, M. Ambrico, V. Augelli, G. Perna, L. Schiavulli, M. A. Tamma, P. F. Biagi, A. Minafra and V. Capozzi, *J. Non-Cryst. Solids*, 2009, **355**, 1221–1226.

4 A. B. Mostert, B. J. Powell, F. L. Pratt, G. R. Hanson, T. Sarna, I. R. Gentle and P. Meredith, *Proc. Natl. Acad. Sci. U. S. A.*, 2012, **109**, 8943–8947.

5 Q. Liu, P. Wang, C. Liu, F. Xue, Q. Wang, Y. Chen, R. Hou and T. Chen, *BMC Neurol.*, 2023, **23**, 301.

6 X. Pan, A. C. Kaminga, S. W. Wen, X. Wu, K. Acheampong and A. Liu, *Front. Aging Neurosci.*, 2019, **11**, 2019.

7 F. A. Zucca, E. Basso, F. A. Cupaioli, E. Ferrari, D. Sulzer, L. Casella and L. Zecca, *Neurotox. Res.*, 2014, **25**, 13–23.

8 Y. Liu, K. Ai and L. Lu, *Chem. Rev.*, 2014, **114**, 5057–5115.

9 H. Lee, S. M. Dellatore, W. M. Miller and P. B. Messersmith, *Science*, 2007, **318**, 426–430.

10 F. Yu, S. Chen, Y. Chen, H. Li, L. Yang, Y. Chen and Y. Yin, *J. Mol. Struct.*, 2010, **982**, 152–161.

11 J. Jeong, J. Do and S. M. Kang, *Adv. Mater. Interfaces*, 2024, **11**, 2300871.

12 H. Khezraqa, S.-A. Safavi-Mirmahalleh, H. Roghani-Mamaqani and M. Salami-Kalajahi, *J. Energy Storage*, 2024, **79**, 110170.

13 C. Zhang, X. Du and Z. Zhang, *Sens. Actuators Rep.*, 2025, **10**, 100348.

14 R. M. Wightman, L. J. May and A. C. Michael, *Anal. Chem.*, 1988, **60**, 769A–770A.

15 A. G. Ewing, J. C. Bigelow and R. M. Wightman, *Science*, 1983, **221**, 169–171.

16 W. G. Kuhr, A. G. Ewing, W. L. Caudill and R. M. Wightman, *J. Neurochem.*, 1984, **43**, 560–569.

17 C. Gu and A. G. Ewing, *Chem. Sci.*, 2021, **12**, 7393–7400.

18 X. Wei, Z. Zhang and Z. Wang, *Microchem. J.*, 2019, **145**, 55–58.

19 R. Pramanik, *Anal. Method.*, 2025, **17**, 4251–4292.

20 A. A. El-Sherbeni, M. R. Stocco, F. B. Wadji and R. F. Tyndale, *J. Chromatogr. A*, 2020, **1627**, 461403.

21 Y. Zhang, S. Qi, Z. Liu, Y. Shi, W. Yue and C. Yi, *Mater. Sci. Eng. C*, 2016, **61**, 207–213.

22 D. P. Zhan, S. N. Mao, Q. Zhao, Z. Chen, H. Hu, P. Jing, M. Q. Zhang, Z. W. Zhu and Y. H. Shao, *Anal. Chem.*, 2004, **76**, 4128–4136.

23 H. D. Jetmore, C. B. Milton, E. S. Anupriya, R. Chen, K. Xu and M. Shen, *Anal. Chem.*, 2021, **93**, 16535–16542.

24 A. Lytvynenko, S. Baluchová, J. Zima, J. Krůšek and K. Schwarzová-Pecková, *Bioelectrochemistry*, 2024, **158**, 108713.

25 M. Sajid, M. K. Nazal, M. Mansha, A. Alsharaa, S. M. S. Jillani and C. Basheer, *Trends Anal. Chem.*, 2016, **76**, 15–29.

26 M. Bilal, Z. U. Rehman, F. K. Butt, Y. Cao, K. Zheng, J. A. Jrar, Z. Zhang and J. Hou, *ACS Appl. Nano Mater.*, 2025, **8**, 9711–9719.

27 F. Weyand, S. Gianvittorio, F. Longo, J. Wang and A. Lesch, *Electrochim. Acta*, 2025, **526**, 146174.

28 A. Pandikumar, G. T. Soon How, T. P. See, F. S. Omar, S. Jayabal, K. Z. Kamali, N. Yusoff, A. Jamil, R. Ramaraj, S. A. John, H. N. Lim and N. M. Huang, *RSC Adv.*, 2014, **4**, 63296–63323.

29 M. Mallesha, R. Manjunatha, C. Nethravathi, G. S. Suresh, M. Rajamathi, J. S. Melo and T. V. Venkatesha, *Bioelectrochemistry*, 2011, **81**, 104–108.

30 A. Cecilia Rossi Fernández, L. Alejandra Meier and N. Jorge Castellani, *Comput. Theor. Chem.*, 2022, **1212**, 113705.

31 E. A. Khudaish and J. A. Rather, *J. Electroanal. Chem.*, 2016, **776**, 206–212.

32 J. Evers, K. Sridhar, J. Liegey, J. Brady, H. Jahns and M. Lowery, *J. Neural Eng.*, 2022, **19**, 046004.

33 P. Limousin and T. Foltynie, *Nat. Rev. Neurol.*, 2019, **15**, 234–242.

34 R. A. Lehane, A. Gamero-Quijano, S. Malijauskaite, A. Holzinger, M. Conroy, F. Laffir, A. Kumar, U. Bangert, K. McGourty and M. D. Scanlon, *J. Am. Chem. Soc.*, 2022, **144**, 4853–4862.

35 R. A. Lehane, A. Gamero-Quijano, J. A. Manzanares and M. D. Scanlon, *J. Am. Chem. Soc.*, 2024, **146**, 28941–28951.

36 K. Lepková, J. Clohessy and V. J. Cunnane, *Electrochim. Acta*, 2008, **53**, 6273–6277.

37 R. Knake, A. W. Fahmi, S. A. M. Tofail, J. Clohessy, M. Mihov and V. J. Cunnane, *Langmuir*, 2005, **21**, 1001–1008.

38 U. Evans-Kennedy, J. Clohessy and V. J. Cunnane, *Macromolecules*, 2004, **37**, 3630–3634.

39 L. Nazari and T. J. Stockmann, *Langmuir*, 2024, **40**, 24494–24506.

40 R. Moshrefi, K. Ryan, E. P. Connors, J. C. Walsh, E. Merschrod, G. J. Bodwell and T. J. Stockmann, *Nanoscale*, 2023, **15**, 5834–5842.

41 R. Moshrefi, H. Przybyła and T. J. Stockmann, *Sci. Rep.*, 2023, **13**, 1201.

42 M. D. Scanlon, E. Smirnov, T. J. Stockmann and P. Peljo, *Chem. Rev.*, 2018, **118**, 3722–3751.

43 R. Moshrefi, E. P. Connors, E. Merschrod and T. J. Stockmann, *Electrochim. Acta*, 2022, **426**, 140749.

44 R. Moshrefi, A. Suryawanshi and T. J. Stockmann, *Electrochem. Commun.*, 2021, **122**, 106894.

45 T. J. Stockmann, P. D. Boyle and Z. Ding, *Catal. Today*, 2017, **295**, 89–94.

46 S. Schindler and T. Bechtold, *J. Electroanal. Chem.*, 2019, **836**, 94–101.

47 A. E. Sánchez-Rivera, S. Corona-Avendaño, G. Alarcón-Angeles, A. Rojas-Hernández, M. T. Ramirez-Silva and M. A. Romero-Romo, *Spectrochim. Acta, Part A*, 2003, **59**, 3193–3203.

48 R. Moshrefi and T. J. Stockmann, *Nanomaterials*, 2022, **12**, 2748.

49 A. Uehara, S.-Y. Chang, S. G. Booth, S. L. M. Schroeder, J. F. W. Mosselmans and R. A. W. Dryfe, *Electrochim. Acta*, 2016, **190**, 997–1006.

50 A. Uehara, S. G. Booth, S. Y. Chang, S. L. M. Schroeder, T. Imai, T. Hashimoto, J. F. W. Mosselmans and R. A. W. Dryfe, *J. Am. Chem. Soc.*, 2015, **137**, 15135–15144.

51 A. Uehara, T. Hashimoto and R. A. W. Dryfe, *Electrochim. Acta*, 2014, **118**, 26–32.

52 T. J. Stockmann, L. Angelé, V. Brasiliense, C. Combellas and F. Kanoufi, *Angew. Chem., Int. Ed.*, 2017, **56**, 13493–13497.

53 T. J. Stockmann, R. Guterman, P. J. Ragogna and Z. Ding, *Langmuir*, 2016, **32**, 12966–12974.

54 A. J. Bard and L. R. Faulkner, *Electrochemical Methods: Fundamentals and Applications*, John Wiley, New York, 2nd edn, 2001.

55 S. Liu, Q. Li and Y. Shao, *Chem. Soc. Rev.*, 2011, **40**, 2236–2253.

56 A. Usher, D. C. McPhail and J. Brugger, *Geochim. Cosmochim. Acta*, 2009, **73**, 3359–3380.

57 M. Luty-Błocho, K. Pacławski, M. Wojnicki and K. Fitzner, *Inorg. Chim. Acta*, 2013, **395**, 189–196.

58 Y. Li, M. Liu, C. Xiang, Q. Xie and S. Yao, *Thin Solid Films*, 2006, **497**, 270–278.

59 J. H. Ryu, P. B. Messersmith and H. Lee, *ACS Appl. Mater. Interfaces*, 2018, **10**, 7523–7540.

60 M. d'Ischia, A. Napolitano, V. Ball, C.-T. Chen and M. J. Buehler, *Acc. Chem. Res.*, 2014, **47**, 3541–3550.

61 N. Nishi, I. Yajima, K.-i. Amano and T. Sakka, *Langmuir*, 2018, **34**, 2441–2447.

62 K. Aoki, *Electroanalysis*, 1993, **5**, 627–639.

63 M. Brust, M. Walker, D. Bethell, D. J. Schiffrin and R. Whyman, *J. Chem. Soc. Chem. Commun.*, 1994, 801–802, DOI: 10.1039/C39940000801.

64 O. F. Odio, L. Lartundo-Rojas, P. Santiago-Jacinto, R. Martínez and E. Reguera, *J. Phys. Chem. C*, 2014, **118**, 2776–2791.

65 Z. Tang, B. Xu, B. Wu, M. W. Germann and G. Wang, *J. Am. Chem. Soc.*, 2010, **132**, 3367–3374.

66 S. Peters, S. Peredkov, M. Neeb, W. Eberhardt and M. Al-Hada, *Surf. Sci.*, 2013, **608**, 129–134.

67 S. Wang, K. Qian, X. Bi and W. Huang, *J. Phys. Chem. C*, 2009, **113**, 6505–6510.

68 J. R. Araujo, B. S. Archanjo, K. R. de Souza, W. Kwapinski, N. P. S. Falcão, E. H. Novotny and C. A. Achete, *Biol. Fertil. Soils*, 2014, **50**, 1223–1232.

69 K. M. Mayer and J. H. Hafner, *Chem. Rev.*, 2011, **111**, 3828–3857.

70 R. S. Nicholson and I. Shain, *Anal. Chem.*, 1964, **36**, 706–723.

71 H.-S. Jang, D. Kim, C. Lee, B. Yan, X. Qin and Y. Piao, *Inorg. Chem. Commun.*, 2019, **105**, 174–181.

72 H. Chen, H. Chen and R. Hong, *Catalysts*, 2019, **9**, 653.

73 S. Anantharaj, P. J. J. Sagayaraj, M. S. Yesupatham, R. Arulraj, K. Eswaran, K. Sekar and S. Noda, *J. Mater. Chem. A*, 2023, **11**, 17699–17709.

74 H. Yang, D. Liu, X. Zhao, J.-H. Yang, H. Chang, R. Xing and S. Liu, *Anal. Method.*, 2017, **9**, 3191–3199.

75 C. Rajkumar, B. Thirumalraj, S.-M. Chen and H.-A. Chen, *J. Colloid Interface Sci.*, 2017, **487**, 149–155.

76 P. Vanýsek, in *CRC Handbook of Chemistry and Physics*, W. M. Haynes, CRC Press/Taylor, Boca Raton, FL, 2021, pp. 20–29.

77 Y. Grunder, H. L. T. Ho, J. F. W. Mosselmans, S. L. M. Schroeder and R. A. W. Dryfe, *Phys. Chem. Chem. Phys.*, 2011, **13**, 15681–15689.

78 J. Anderson, S. Sawtelle and C. McAndrews, *Inorg. Chem.*, 1990, **29**, 2627–2633.

79 D. J. Fermin and R. Lahtinen, in *Liquid Interfaces in Chemical, Biological and Pharmaceutical Applications*, A. G. Volkov, Marcel Dekker, Inc., 2001, vol. 8.

80 M. A. Méndez, R. Partovi-Nia, I. Hatay, B. Su, P. Y. Ge, A. Olaya, N. Younan, M. Hojeij and H. H. Girault, *Phys. Chem. Chem. Phys.*, 2010, **12**, 15163–15171.

81 R. Ciganda, J. Irigoyen, D. Gregurec, R. Hernández, S. Moya, C. Wang, J. Ruiz and D. Astruc, *Inorg. Chem.*, 2016, **55**, 6361–6363.

82 G. A. Mabbott, *J. Chem. Educ.*, 1983, **60**, 697.

83 S. Corona-Avendaño, G. Alarcón-Angeles, M. T. Ramírez-Silva, G. Rosquete-Pina, M. Romero-Romo and M. Palomar-Pardavé, *J. Electroanal. Chem.*, 2007, **609**, 17–26.

84 F. Zhang and G. Dryhurst, *Bioorg. Chem.*, 1993, **21**, 392–410.

85 D. A. Skoog, F. J. Holler and S. Crouch, *Principles of Instrumental Analysis*, Thomson Higher Education, Belmont, CA, 6th edn, 2007.

86 K. Zhang, H. Wu and Y. Zhang, *Int. J. Electrochem. Sci.*, 2022, **17**, 220662.

87 X. Liu and J. Liu, *VIEW*, 2021, **2**, 20200102.

88 A. Karim, M. Yasser, A. Ahmad, H. Natsir, A. Wahid Wahab, S. Fauziah, P. Taba, I. Pratama, Rosalin, A. Rajab, A. Nur Fitriani Abubakar, T. Widayati Putri, R. Munadi, A. Fudhail Majid, A. Nur Fadliah, A. Rifai and M. Syahrir, *J. Electroanal. Chem.*, 2024, **959**, 118157.

89 R. Wu, S. Yu, S. Chen, Y. Dang, S.-H. Wen, J. Tang, Y. Zhou and J.-J. Zhu, *Anal. Chim. Acta*, 2022, **1229**, 340365.

90 P. Ramu, S. P. Vimal, P. Suresh, A. Sanmugam, U. Saravanakumar, R. S. Kumar, A. I. Almansour, N. Arumugam and D. Vikraman, *RSC Adv.*, 2022, **12**, 15575–15583.

91 M. Harsini, B. A. Widyaningrum, E. Fitriany, D. R. A. Paramita, A. N. Farida, A. Baktir, F. Kurniawan and S. C. W. Sakti, *Chin. J. Anal. Chem.*, 2022, **50**, 100052.

92 A. R. M. Rosli, M. S. Noorashikin and F. Yusoff, *J. Electrochem. Soc.*, 2021, **168**, 087512.

93 Y. Zhang and S. Luo, *J. Electrochem. Soc.*, 2025, **172**, 057501.